Phase diagram of $BiFeO_3/LaFeO_3$ superlattices studied by x-ray diffraction experiments and first-principles calculations

Gijsbert Rispens and Benedikt Ziegler
DPMC-MaNEP, Université de Genève, Quai Ernest-Ansermet 24, 1211 Geneva, Switzerland

Zeila Zanolli*
Physique Théorique des Matériaux, Université de Liège, B-4000 Sart Tilman, Belgium and European Theoretical Spectroscopy Facility (ETSF)

Jorge Íñiguez
Institut de Ciència de Materials de Barcelona (ICMAB-CSIC), Campus UAB, 08193 Bellaterra, Spain

Philippe Ghosez
Theoretical Material Physics, Université de Liège (B5a), B4000 Sart Tilman, Belgium

Patrycja Paruch†
DPMC-MaNEP, Université de Genève, Quai Ernest-Ansermet 24, 1211 Geneva, Switzerland

(Received 2 July 2013; revised manuscript received 8 August 2014; published 12 September 2014; corrected 13 October 2014)

Combining structural and functional measurements, we have mapped the phase diagram of $BiFeO_3/LaFeO_3$ superlattices grown by off-axis sputtering on $(110)_o$ $DyScO_3$ substrates. The phase diagram displays three distinct regions as a function of $BiFeO_3$ fraction, with a $BiFeO_3$-like ferroelectric phase and a $LaFeO_3$-like paraelectric phase at its extremities, and a complex intermediate region, as supported by first-principles calculations. This intermediate region shows unusual, mixed functional behavior, most likely due to competing phases driven by substitution with a same-size central ion and the specific boundary conditions imposed by the superlattice structure. In the $BiFeO_3$ rich superlattices, scaling of the ferroelectric-to-paraelectric transition temperature with the $BiFeO_3$ thickness could provide an alternate route for studying ferroelectric size effects in $BiFeO_3$.

DOI: 10.1103/PhysRevB.90.104106 PACS number(s): 77.55.Px, 77.80.bg, 77.55.Nv, 68.65.Cd

I. INTRODUCTION

In superlattices of ferroelectric and dielectric perovskites, the interplay between the ferroelectric polarization and the rotation of the oxygen octahedra, coupled with the electrostatic and epitaxial strain boundary conditions imposed by the superlattice structure and the substrate, provides almost endless possibilities for tuning of the functional properties of these "artificial materials" [1–5]. Moreover, in some cases nanoscale phenomena such as interface effects [6–8] and ferroelectric size effects [9–11] can lead to enhanced or unusual responses. Recently, first-principles calculations [12] have shown that short period $BiFeO_3/LaFeO_3$ superlattices exhibit hybrid improper ferroelectricity and magnetism, and that electric control of magnetization is possible in such a system. $BiFeO_3/LaFeO_3$ is a particularly interesting ferroelectric-paraelectric system, hitherto not experimentally studied in superlattice form.

Since the ionic radii of Bi^{3+} and La^{3+} in 12-fold coordination are the same [13,14], the main difference between the two ions is the 6*s* lone electron pair of Bi^{3+}, responsible for the ferroelectricity in $BiFeO_3$. The superlattices can therefore be considered as consisting of $BiFeO_3$ and "$BiFeO_3$ without ferroelectricity," providing a closer match than, for example, Pb and Sr, Ba and Sr, or Bi and Sr. Moreover, as the rotations of the oxygen octahedra are coupled to the cation displacements, where bulk ferroelectric $BiFeO_3$ has a rhombohedral ($R3c$) structure [15] with an $a^-a^-a^-$ rotation pattern in Glazer's notation [16], bulk $LaFeO_3$ has an orthorhombic ($Pnma$) structure with an $a^-a^-c^+$ rotation pattern [17]. Thus, in contrast to many other superlattices, the properties in the coupled $BiFeO_3/LaFeO_3$ system should be driven by electronic effects rather than chemical pressure. However, we note that in thin film form, $BiFeO_3$ presents a slight monoclinic distortion as a result of substrate induced strain—such films are generally referred to as "rhombohedral-like" [14]. Finally, the superlattice is multiferroic [12] with $BiFeO_3$ [14] and $LaFeO_3$ both exhibiting *G*-type antiferromagetic structure. Hence, from an experimental viewpoint, this most probably translates primarily to the suppression of the incommensurate cycloid structure of the bulk material, as already observed in the $BiFeO_3$-$LaFeO_3$ solid solution [18] and $BiFeO_3$ thin films [19].

Recent experimental and theoretical results on solid solutions of $BiFeO_3$ and $LaFeO_3$ illustrate some aspects of this complex behavior, with morphotropic-boundary-like characteristics [20], incommensurability [21], and anomalous magnetostriction [22] observed at different compositions. More generally, the solid solutions present an extremely rich phase diagram with reports of various, sometimes competing, structures between those of the two parent materials [20–26]. $BiFeO_3/LaFeO_3$ *superlattices* would thus be particularly useful in separating out the microscopic mechanisms behind this structural complexity—intermixing vs strain vs electrostatic effects vs composition—and relating them to the functional behavior of the system.

*Present address: PGI and IAS, Forschungszentrum Jülich, D-52425 Jülich, Germany.
†patrycja.paruch@unige.ch

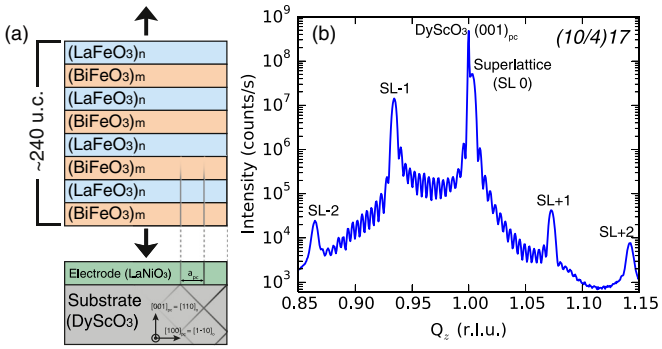

FIG. 1. (Color online) (a) Schematic representation of the superlattices with m $BiFeO_3$ and n $LaFeO_3$ (pseudocubic) lattice units, and p periods in the full superlattice. (b) Specular x-ray diffraction from a typical superlattice on $(110)_o$ $DyScO_3$ confirming high crystalline quality.

In this paper, we report on such a study, where the growth of high quality epitaxial $BiFeO_3/LaFeO_3$ superlattices allowed a detailed investigation of its phase diagram, mapping out the dependence of the structural and functional properties on the $BiFeO_3$ fraction and superlattice period.

II. MATERIALS AND METHODS

$[(BiFeO_3)_m/(LaFeO_3)_n]_p$ superlattices were grown on $(110)_o$ $DyScO_3$ substrates by off-axis RF magnetron sputtering from 1.3 in. *Praxair* targets, on $LaNiO_3$ electrodes when appropriate for functional measurements. An Ar/O_2 ratio of 4/1 at a gas pressure of 100 mTorr, and RF powers of 50 W, 40 W, and 50 W were used for $BiFeO_3$, $LaFeO_3$, and $LaNiO_3$, respectively. X-ray diffraction (XRD) measurements were conducted in a *Panalytical* MRD 4 circle diffractometer (Cu-$K\alpha$ radiation), with an *Anton Paar DSH900* domed hotstage mounted for temperature measurements. Synchrotron XRD measurements (energy: 10.5 keV) were conducted at the W1 beamline at Hasylab in Hamburg. An *Agilent* 4284a LCR meter and an *Aixacct* TF2000 analyzer were used for the dielectric and ferroelectric characterization, respectively.

The superlattices are denoted by $(m/n)p$, where m and n are the number of (pseudocubic) unit cell layers of $BiFeO_3$ and $LaFeO_3$, respectively, and p is the number of periods in the full superlattice structure. As shown schematically in Fig. 1(a), in all samples we deposited $BiFeO_3$ as the bottom layer of the superlattice, and the overall superlattice thickness was approximately 240 (pseudocubic) unit cells, depending on the period. Superlattice structure varied from very short period samples to longer periods, for example from $m = 4$, $n = 1$ to $m = 21$, $n = 7$ for the same $BiFeO_3$ volume fraction of 0.80. The lattice match between the $(110)_o$ $DyScO_3$ substrate and the superlattice is quite good (see Table I), allowing growth of fully strained samples. However, to prevent relaxation of the highly strained $LaNiO_3$, very thin electrode layers (≈4 nm) were deposited. The superlattices are of high crystalline quality as demonstrated by the presence of superstructure peaks and finite size oscillations in the x-ray diffraction (XRD) measurements, such as those shown in Fig. 1(b) for a (10/4)17 superlattice.

TABLE I. Pseudocubic lattice parameters for bulk rhombohedral (R) and orthorhombic (O) superlattice component materials, with α denoting the rhombohedral angle, or the angle between the pseudocubic a and c lattice vectors, respectively.

	$BiFeO_3$	$LaFeO_3$	$LaNiO_3$	$DyScO_3$
a_{pc} (Å)	3.965	3.931	3.838	3.943
b_{pc} (Å)	3.965	3.913	3.838	3.945
c_{pc} (Å)	3.965	3.931	3.838	3.943
$\alpha(^\circ)$	89.3(R)	89.9(O)	89.3(R)	87.2(O)

III. RESULTS AND DISCUSSION

The two key parameters for mapping the behavior of any superlattice system are the overall composition and the superlattice period. To allow direct comparison of our results to the observations made in $BiFeO_3/LaFeO_3$ solid solutions, we chose overall composition as the primary variable.

A. Structural characterization by x-ray diffraction

First, from measurement of the average out-of-plane lattice parameter as a function of $BiFeO_3$ fraction, we observe a well-defined step at a fraction of approximately 0.75, as can be seen in Fig. 2(a) for two different superlattice series with $(m + p)$ periods of 20 and 12 unit cells, respectively. The average lattice parameters were determined either from a Gaussian fit of the most intense superlattice peak or by simulating the target (tetragonal) superlattice (with substrate) diffraction pattern based on a simple kinematical model. The vertical error bars correspond to the range where the fit was visually feasible. Since reciprocal space maps on both sides of this step [Figs. 2(b) and 2(c)] show that coherence with the substrate is fully maintained in each case, the long axis of the average superlattice unit cell thus changes from out-of-plane to in-plane. Moreover, the very discrete nature of the step indicates that there is no continuous path between the two structures. Therefore, the superlattices undergo a structural phase transition as a function of $BiFeO_3$ fraction, at which, from purely structural considerations, the ferroelectric polarization must either be suppressed, or change its orientation. At such a first-order-like transition a region of coexistence between the two phases may be expected, and is indeed observed for a number of "mixed" samples. The appearance of coexistence and the ratio between the two phases seems to depend on the superlattice period and growth as well as the annealing conditions. In particular, the intensity ratio between the diffraction peaks representing the two phases can be modified in a given mixed sample simply by cooling from the paraelectric phase at different rates.

B. Comparison with first-principles calculations

This result has been confirmed by first-principle spin-polarized calculations performed using the VASP [27] implementation of density functional theory (DFT). We employed the projected augmented wave (PAW) method [28] and the PBEsol functional [29], including the rotationally invariant U correction [30], with $U = 4.5$ eV and $J = 0.5$ eV for the Fe-ion on-site Coulomb and exchange parameters, respectively. These values for the U and J parameters accurately describe the properties of the $(BiFeO_3)_1/(LaFeO_3)_1$ superlattice strained to $SrTiO_3$ [12]. Convergence studies

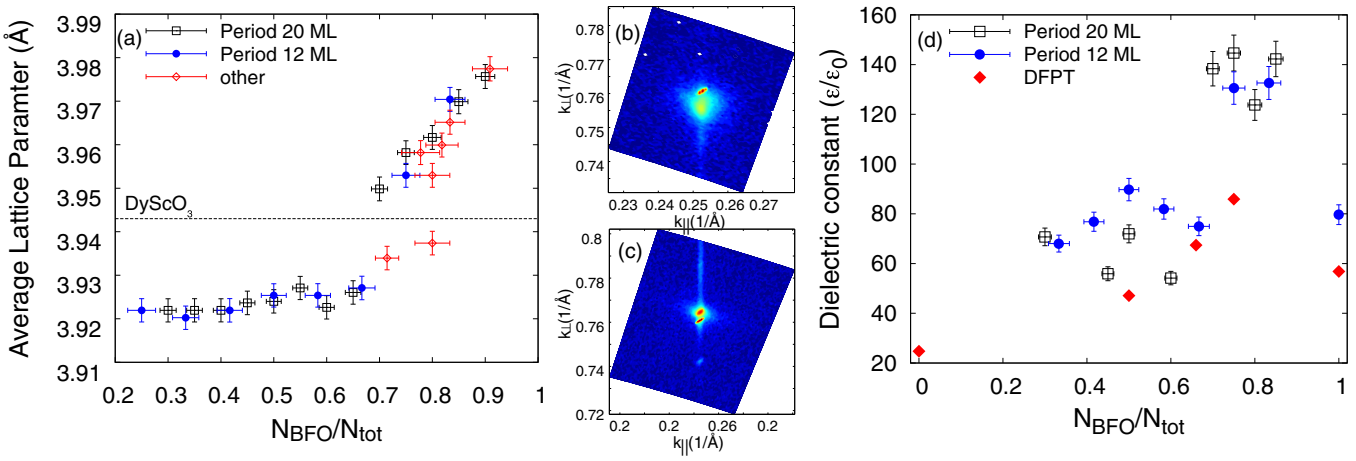

FIG. 2. (Color online) (a) Evolution of average out-of-plane lattice parameter with overall $BiFeO_3$ fraction for two series of superlattices with 12 and 20 unit cell periods, respectively. (b),(c) Reciprocal space maps around the $(332)_o$ reflection of $DyScO_3$ for superlattices with a large and a small out-of-plane average lattice parameter, showing that the superlattices are fully strained throughout the phase diagram. (d) Evolution of the dielectric constant with overall $BiFeO_3$ fraction for the same two series of superlattices and the DFPT model. The dielectric constant peaks on the $BiFeO_3$-rich side of the lattice parameter step.

lead to a kinetic energy cutoff of 500 eV. The Brillouin zone was sampled by a Γ-centered Monkhorst-Pack mesh equivalent to an $8 \times 8 \times 4$ k mesh for a 20 atom cell of the $(BiFeO_3)_1/(LaFeO_3)_1$ superlattice. Atomic positions were relaxed until the maximal force was smaller than 0.5×10^{-3} eV/Å. Cell parameters were relaxed imposing solely the in-plane epitaxial strain. The rotations in the two materials were allowed to relax within each plane. The computational setup was tested on bulk $BiFeO_3$, $LaFeO_3$, and $DyScO_3$, finding unit cell parameters close to the experimentally determined values, as can be seen in Tables I and II.

The epitaxial constraint due to the $(110)_o$ $DyScO_3$ substrate was imposed by fixing the in-plane lattice constant of the $BiFeO_3/LaFeO_3$ superlattices (3.891 Å) to the lattice constant of $DyScO_3$ relaxed from first principles, resulting in a strain of 1.1%. We simulated superlattices with different $BiFeO_3$ fractions by modeling a range of compositions: $(BiFeO_3)_m/(LaFeO_3)_n$ with $m = n = 2$ (0.5), $m = 4$, $n = 2$ (0.66), $m = 3, n = 1$ (0.75), and $m = 5, n = 1$ (0.83). For each system, we compared the total energy of structures that were initially in the polar $R3c$ ($a^-a^-a^-$) and the nonpolar $Pnma$ ($a^-a^-c^+$) phase. After relaxation the tilt pattern (reported in the Appendix for the most stable structures) changes only slightly in the regime with $BiFeO_3$ fractions smaller than 0.80; hence we call the relaxed phases $R3c$-like and $Pnma$-like, the latter being always the most stable. In contrast, the relaxed structures with $BiFeO_3$ content higher than 75% show a more complex rotation pattern that cannot be described as $a^-a^-a^-$ or $a^-a^-c^+$. In this case we have an intermediate situation where the rotation angle evolves smoothly from one layer to the next one (see the Appendix for details). This phase acts as a bridge between the in-phase (observed for $N_{BFO}/N_{tot} < 0.8$) and antiphase (corresponding to pure $BiFeO_3$) rotation patterns about the out-of-plane direction. The energy difference between the $Pnma$-like and $R3c$-like structures diminishes with increasing $BiFeO_3$ fraction and, for $BiFeO_3$ content beyond 0.75, the structure relaxed starting from the $a^-a^-a^-$ pattern becomes energetically more favorable (inset of Fig. 3). The computed values of the out-of-plane lattice constant as a function of $BiFeO_3$ fraction are reported in Fig. 3; at each composition, we show the result for the most stable structure.

TABLE II. Pseudocubic lattice parameters of bulk $BiFeO_3$ (rhombohedral), $LaFeO_3$, and $DyScO_3$ computed from first principles (PBEsol + U). α is the angle (in degrees) between the pseudocubic lattice parameters. The lattice parameters of $DyScO_3$ in the $(110)_o$ plane are a_{pc} and c_{pc}.

PBEsol + U	$BiFeO_3$	$LaFeO_3$	$DyScO_3$
a_{pc} (Å)	3.969	3.902	3.936
b_{pc} (Å)	3.969	3.934	3.920
c_{pc} (Å)	3.969	3.907	3.936
α(°)	89.57		

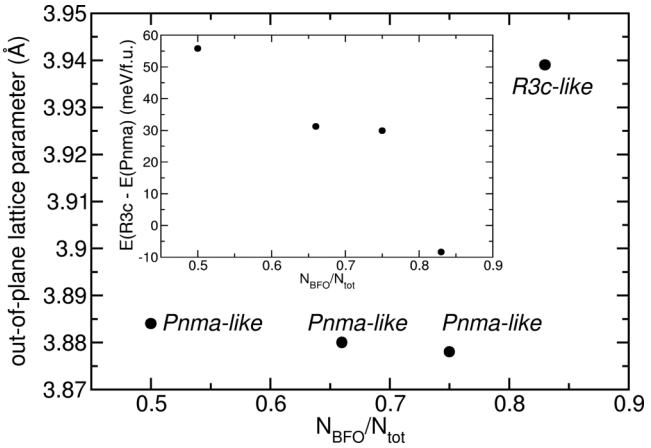

FIG. 3. Out-of-plane lattice parameter from PBEsol + U calculations for superlattices with varying fraction of $BiFeO_3$. For $BiFeO_3$ fractions below 0.8 the $Pnma$-like (initial structure $a^-a^-c^+$) phase is favored over the $R3c$-like (initial structure $a^-a^-a^-$) phase (inset), resulting in a sharp change of lattice parameter.

This result is in line with the experimental finding of an intermediate region where both phases coexist, and explains the step in the out-of-plane lattice constant observed in x-ray diffraction as due to an abrupt change in the symmetry of the structure with increasing $BiFeO_3$ content. However, we note that simply x-ray diffraction measurements do not readily allow access to the oxygen rotations associated with the numerically simulated structures. A more local atomistic-resolution technique such as transmission electron microscopy would allow a better comparison between the experimental and theoretical structures.

Even though the first principles calculations were performed for the shortest possible superlattice period, our results can be generalized to long period superlattices. Further calculations performed for superlattices with fixed composition and different layer thickness, moreover, show that the most stable energy structure is determined by the average composition, with the layer thickness playing a minor role.

C. Dielectric measurements

A structural ferroelectric phase transition is normally also accompanied by an enhancement of the dielectric response. However, although the dielectric constant is enhanced close to the 0.75 $BiFeO_3$ fraction boundary, the enhancement is quite modest, as can be seen in Fig. 2(d). Moreover, the dielectric response is only enhanced on the $BiFeO_3$-rich side of the boundary, instead of at the (paraelectric) $LaFeO_3$ side, where the largest enhancement would in fact be expected for a typical first-order ferroelectric transition.

To better understand our dielectric measurements, we modeled the SLs as a series of $BiFeO_3$ and $LaFeO_3$ capacitors. Using density functional perturbation theory methods, we computed from first principles the static dielectric response of the pure $BiFeO_3$ and $LaFeO_3$ materials, strained to match a $DyScO_3$ substrate, in the rhombohedral ($a^-a^-a^-$) and orthorhombic ($a^-a^-c^+$) phases. The results are reported in Table III. The dielectric constant of the SL is then given by

$$\epsilon = \frac{\epsilon_{BFO}\epsilon_{LFO}(d_{BFO} + d_{LFO})}{d_{LFO}\epsilon_{BFO} + d_{BFO}\epsilon_{LFO}}, \quad (1)$$

where d_{BFO} and d_{LFO} are the thicknesses of $BiFeO_3$ and $LaFeO_3$ layers.

In the $N_{BFO}/N_{tot} < 0.8$ regime the relaxed SL has a $a^-a^-c^+$ tilt pattern, as can be seen from the oxygen octahedra rotations collected in the Appendix. Hence the dielectric constants of $BiFeO_3$ and $LaFeO_3$ in the orthorhombic phase can be used to estimate ϵ. The results of this model are shown in Fig. 2(d) and indicate that a larger $BiFeO_3$ content leads to a moderate increase of the SL dielectric constant (because of the large value of the computed dielectric constant for $BiFeO_3$ in the *Pnma* phase), in agreement with the experimental trend.

TABLE III. Static dielectric constant for bulk $BiFeO_3$ and $LaFeO_3$ strained to $DyScO_3$ in the rhombohedral ($a^-a^-a^-$) and orthorhombic ($a^-a^-c^+$) phases computed from first principles.

Dielectric constant ϵ_{zz}/ϵ_0	$a^-a^-a^-$	$a^-a^-c^+$
$BiFeO_3$	57	490
$LaFeO_3$	42	25

The rotation pattern of the $(BiFeO_3)_5/(LaFeO_3)_1$ superlattice (Appendix) includes both in-phase and anti-phase rotations about z, with different rotation angles for each octahedron layer. A capacitor model based on results for phases with purely $a^-a^-a^-$ or $a^-a^-c^+$ rotation patterns is, therefore, not appropriate to model the dielectric constant of this complex phase or to describe the experimentally observed enhancement of the dielectric constant for $N_{BFO}/N_{tot} \sim 0.8$.

To further study the nature of the different structural phases observed via XRD, we then probed the dielectric and ferroelectric properties of the superlattices in more detail, with measurements carried out at 15 K to minimize leakage. Superlattices with a large out-of-plane lattice parameter show normal ferroelectric behavior, similar to that of pure $BiFeO_3$ thin films, while $LaFeO_3$-rich superlattices are paraelectric [Figs. 4(a) and 4(b)]. However, between these two extremes there is a region of more complex behavior, in which polarization-voltage (P-V) hysteresis resembles a combination of paraelectric and ferroelectric responses [Fig. 4(c)]. At the same time, the capacitance-voltage (C-V) characteristics show a quadruple-humped curve for lower voltages resembling those of an antiferroelectric [31] [Fig. 4(d)]. Similar C-V (ϵ-E) characteristics in other rare-earth doped $BiFeO_3$ solid solutions were attributed to an electric-field-induced structural transformation from the orthorhombic to rhombohedral phase [32]. The proximity in energy of the nonpolar *Pnma*-like and polar *R*3*c*-like phases in the intermediate region and the possibility of a field-induced first-order phase transition between them provides the basic ingredients for an antiferroelectric behavior as recently argued by Rabe [33]. Interestingly, applying high dc voltages (>35 V) to these samples leads to ferroelectriclike C-V dependence. This forming procedure roughly doubles the dielectric constant, to a value of around 150, similar to that measured in the ferroelectric samples near the phase boundary. The magnitude of the field-induced polarization is likewise similar for the ferroelectric and the intermediate (0.45–0.8 $BiFeO_3$) region samples, as can be seen when comparing Figs. 4(a) and 4(c).

These observations suggest that in the intermediate region samples, high electric fields stabilize a phase similar to the stable ferroelectric phase for $BiFeO_3$-rich samples. Although we have seen irreversible switching to this ferroelectric phase in a limited number of samples, in most cases the original behavior is slowly recovered once the field is removed.

D. Half-order peaks

Coinciding with the complex functional behavior, broad half-order (cell doubling) diffraction peaks are observed in superlattices with an overall $BiFeO_3$ fraction between 0.45 and 0.8, an example of which can be seen in Fig. 5(a). From their large width, finite size estimates suggest that this cell doubling appears in a thin layer somewhere within the superlattice, although other effects could also contribute to the observed broadening. To clarify the nature of these half-order peaks, we conducted temperature-dependent XRD measurements, which showed that the peaks disappear above 550 °C, and reappear again at their original position upon cooling, as can be seen

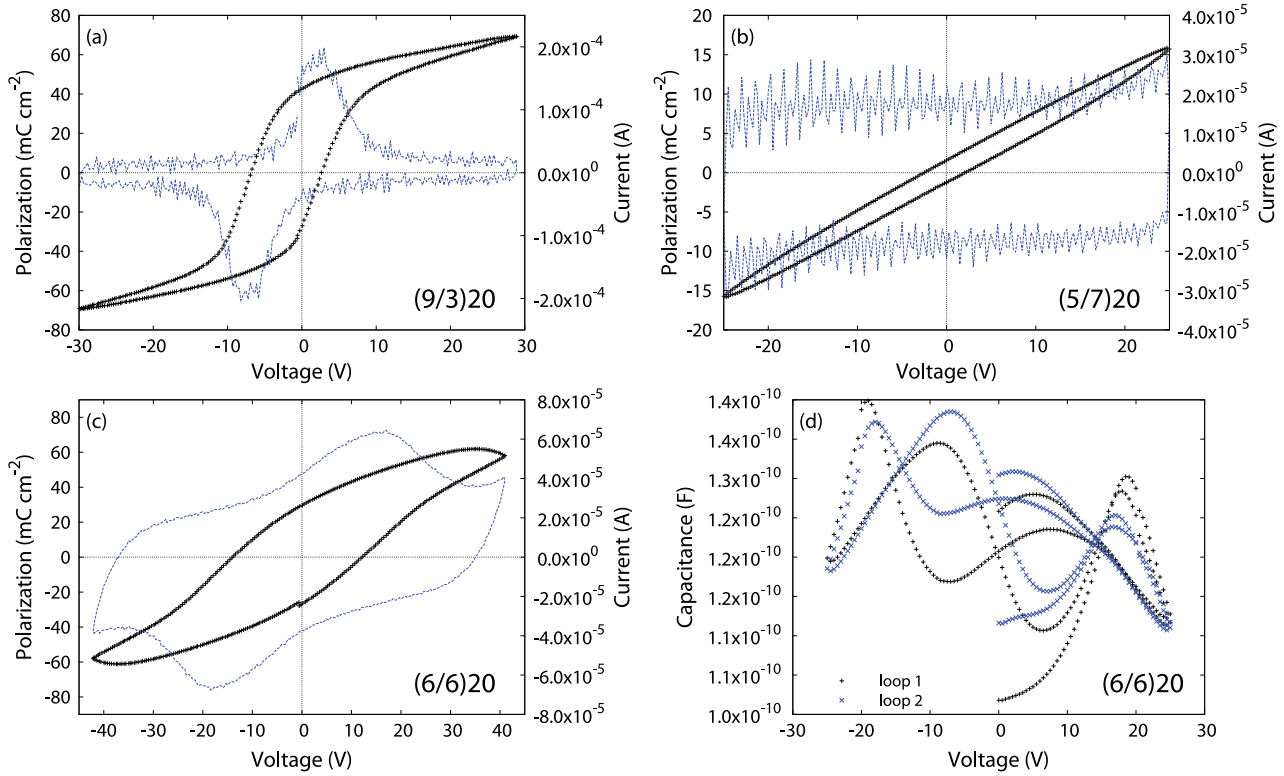

FIG. 4. (Color online) Polarization-voltage (P-V) dependence showing (a) normal ferroelectric behavior for a (9/3)20 superlattice, (b) paraelectric behavior for a (5/7)20 superlattice, and (c) mixed ferroelectric-paraelectric behavior for a (6/6)20 superlattice. (d) Capacitance-voltage measurement for the same superlattice showing complex behavior with a quadruple-humped curve.

in Fig. 5(b). This temperature dependence, and the range of $BiFeO_3$ fractions where the half-order peaks are observed, combined with the distinct functional properties present for these samples, clearly define a separate region in the phase diagram of the $BiFeO_3/LaFeO_3$ superlattice system. However, the complex functional response and the large width of the half-order peaks suggest that the complex behavior in this region may in fact not be due to only a single phase, but rather to competing effects of a number of different but structurally and energetically similar phases.

Such a hypothesis is consistent with recent first-principles predictions that $BiFeO_3$ and related materials present so-called *nanoscale twinned phases*, which can be viewed as a mixture of the $R3c$ and $Pnma$ structures [34]. Such phases display the regular antiphase (i.e., a^-a^--like) octahedral rotations in a (001)-equivalent plane, but show a longer-period modulation of the O_6 tilts along the third pseudocubic direction, thus constituting a *structural bridge* between the $a^-a^-a^-$ and $a^-a^-c^+$ limit cases. The calculations also predict that unconventional antiferroelectric orders appear as the result of the complex tilting patterns. To test whether such structures can potentially occur in $BiFeO_3/LaFeO_3$ superlattices, we ran first-principles simulations for the most stable nanotwinned phases of Ref. [34] and various layer stackings spanning the compositions of interest. For computational feasibility, we considered the Bi/La stacking to occur along the direction

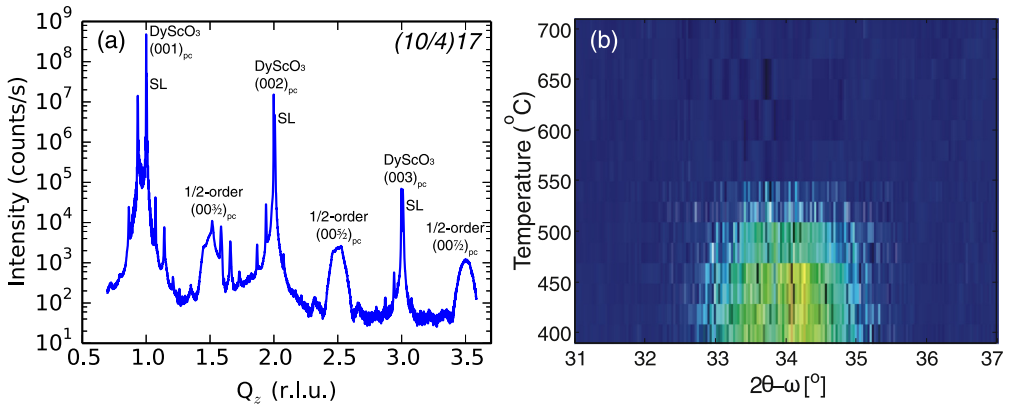

FIG. 5. (Color online) (a) Synchrotron XRD measurement along the specular rod, showing the presence of half-order (cell doubling) peaks. (b) Temperature dependence of such half-order peaks. The peaks reappear at the same position upon cooling.

of the complex rotation pattern; this amounts to considering (001)-oriented superlattices for which $DyScO_3$-like epitaxial conditions were imposed. Interestingly, we found that in this case the $R3c$-like to $Pnma$-like transition occurs for a $BiFeO_3$ content of about 0.7. Further, in the transition region, the longer-period structures with complex tiltings become very competitive in energy, lying less than 10 meV/f.u. above the ground state. These results clearly support the notion that phase competition and coexistence, as well as complex longer-period structures, can occur in the intermediate composition region of the $BiFeO_3/LaFeO_3$ superlattices.

Alternatively, these half-order peaks could originate from spatial polarization and rotation inhomogeneities leading to flexo-antiferrodistortive coupling, which has been shown to promote modulated structures [35].

Taken together, these results delineate an emerging phase diagram at room temperature, which seems to consist of three different regions depending on the $BiFeO_3$ fraction. The regions closest to the pure materials behave similarly to $BiFeO_3$ or $LaFeO_3$ thin films, respectively, while the intermediate region shows complex, possibly mixed behavior.

E. Temperature-dependent x-ray diffraction measurements

To map the temperature axis of the phase diagram, we then measured the structural distortion with respect to the paraelectric phase as a function of temperature using XRD. This distortion is calculated by subtracting the paraelectric lattice parameter, obtained by linear extrapolation from the high-temperature phase, from the average lattice parameter. We assume this high-temperature phase to have an orthorhombic structure with $a^-a^-c^+$ rotations similar to $LaFeO_3$ and the β phase of $BiFeO_3$ [36]. Superlattices with high $BiFeO_3$ fraction show a roughly linear decrease of the distortion at lower temperatures, followed by a sharp transition into the high temperature (paraelectric) phase, as can be seen in Fig. 6(a) for a superlattice with 0.8 $BiFeO_3$ fraction. If the superlattice period is decreased, while maintaining the overall $BiFeO_3$ fraction constant, the transition temperature (T_C) is reduced. However, for superlattices with different $BiFeO_3$ fractions, but identical thicknesses of the $BiFeO_3$ sublayer, T_C is almost constant, and although the magnitude of the distortion changes, the shape of the curve remains the same. Thus, for the $BiFeO_3$-rich superlattices, the reduction of T_C scales with the thickness of the $BiFeO_3$ sublayer, almost linearly from a (21/7)8 down to a (4/1)48 superlattice [Fig. 6(d)]. The appearance of such a ferroelectric size effect suggests that the ferroelectric polarization does not couple between the different $BiFeO_3$ sublayers, even for low $LaFeO_3$ thicknesses.

Meanwhile, the distortion of a (5/5)24 superlattice, as shown in Fig. 6(b), has significantly different behavior, with a linear decrease of the distortion towards zero, resembling a

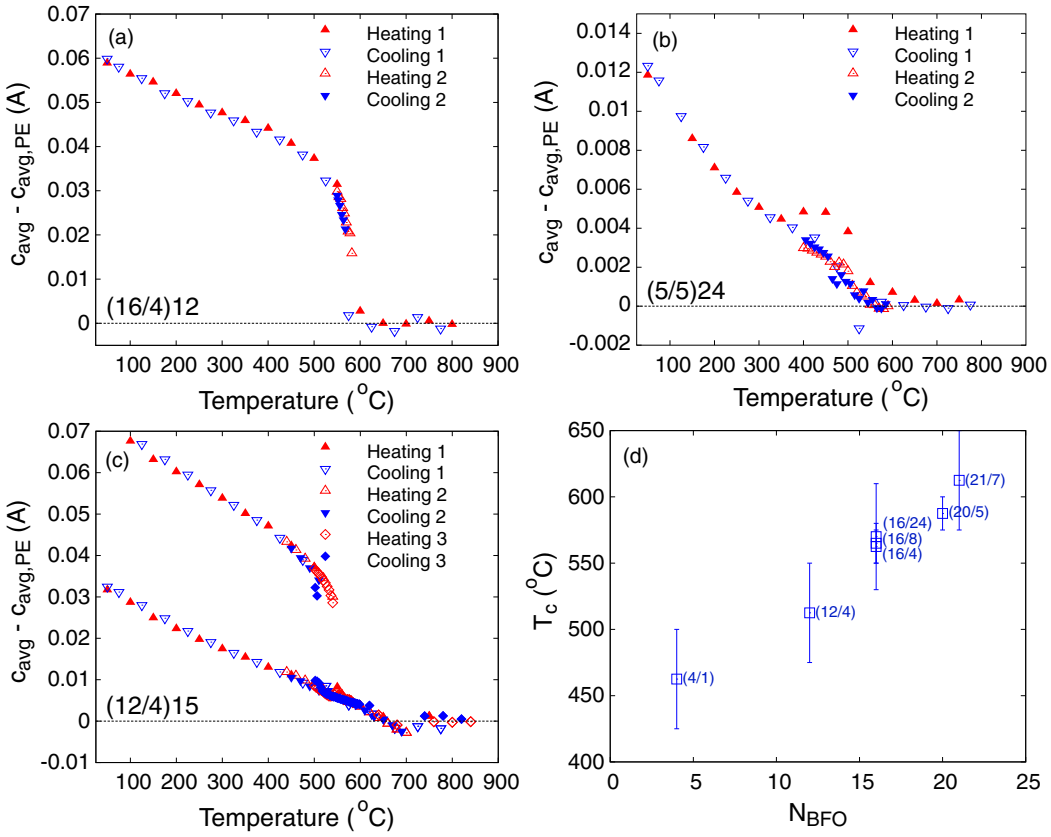

FIG. 6. (Color online) Evolution with temperature of the difference between the average lattice parameter and the paraelectric lattice parameter (obtained from a linear fit of the high temperature data) for (a) (16/4)12, (b) (5/5)24, and (c) (12/4)15 superlattices, showing two distinct out-of-plane lattice parameters. (d) The transition temperature T_C scales linearly with the $BiFeO_3$ sublayer thickness. The error bars are a measure of the observed thermal hysteresis.

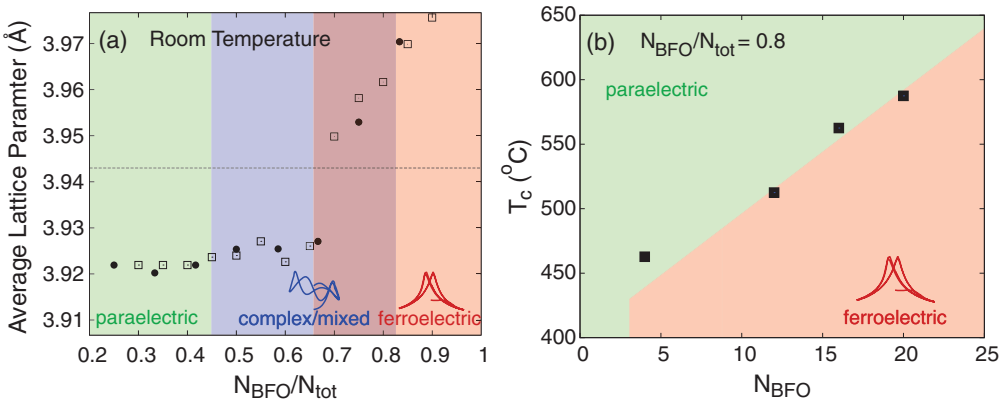

FIG. 7. (Color online) Schematic phase diagram of $BiFeO_3/LaFeO_3$ superlattices on (110)$DyScO_3$ substrates. (a) Room temperature phase diagram as a function of $BiFeO_3$ fraction. There are three distinct regions: a $BiFeO_3$-like region, a $LaFeO_3$ region, and a rich and complex intermediate region. (b) Phase diagram as a function of $BiFeO_3$ thickness per period for a $BiFeO_3$ fraction of 0.8. The transition temperature scales linear with $BiFeO_3$ thickness.

second-order phase transition. In mixed superlattices where two distinct lattice parameters are present, both the sharp and the continuous phase transition are observed, as can be seen in Fig. 6(c). At the first (sharp) transition there is a clear improvement of the Laue oscillations in the XRD scans, indicating that the system collapses into a single phase before undergoing the second transition. Thus, for this (12/4)15 superlattice, the sharp transition is not directly into the high temperature phase. Upon cooling, the superlattice undergoes the reverse sequence of phase transitions, although the XRD intensity ratio, and thus the phase fractions, may vary depending on the cooling conditions.

While the nature of the second phase transition and the associated distortion is not yet completely clear, and there are significant sample-to-sample variations, the region where the superlattices show this transition nonetheless appears to coincide with the region where the half-order peaks are observed. The extremely complex functional behavior of the superlattices in this region of the phase diagram renders assigning the distortion to a specific mechanism difficult, based on the available data. Moreover, the observed variation indicates that this behavior is sensitive to small differences in growth rate, and thus in the interface quality, inherent to off-axis sputtering, in turn suggesting that the interface may play an important role in this phase transition.

TABLE IV. Rotation angles in the $(BiFeO_3)_2/(LaFeO_3)_2$ superlattice ($N_{BFO}/N_{tot} = 0.50$) with tilt pattern $a^-a^-c^+$. We use the label "BFO" to denote octahedra centered at Fe atoms within a FeO_2 plane placed between two BiO planes, "LFO" to denote octahedra centered at Fe atoms within a FeO_2 plane placed between two LaO planes, and "interface" to denote the case in which the FeO_2 plane is placed between LaO and BiO planes.

Octahedron	Angle x	Angle y	Angle z
1 (BFO)	10.6	10.6	11.1
2 (interface)	10.0	9.9	9.4
3 (LFO)	9.2	9.1	7.61
4 (interface)	10.0	9.9	9.4

We note that while the structural measurements were carried out up to 750 °C, the functional measurements were performed at 4 K. A phase transition in the intervening temperature range, while not imaged structurally, should nonetheless be identifiable, for example by discontinuities in the dielectric susceptibility behavior. We did not observe such signatures, and thus believe that the first-principles calculations are a good qualitative reflection of the higher-temperature situation. In addition, a reasonable match is found between modeling and experiment if the thermal expansion close to room temperature is extrapolated to 0 K.

IV. CONCLUSIONS

In summary, we can describe the room temperature behavior of $BiFeO_3/LaFeO_3$ superlattices grown on $(110)_o$ $DyScO_3$ as a function of the overall $BiFeO_3$ fraction, allowing us to delineate a phase diagram in which three distinct regions are observed: a ferroelectric region with behavior similar to that of pure $BiFeO_3$ thin films, a paraelectric region with properties resembling those of $LaFeO_3$ thin films, and an intermediate region showing more complex functional behavior (see Fig. 7), in excellent agreement with first principles calculations. The intermediate region is also characterized by wide half-order peaks and what appears to be a structural distortion that undergoes a second order phase transition at high temperature. Between the $BiFeO_3$-like and the intermediate phases, there is

TABLE V. Rotation angles in the $(BiFeO_3)_4/(LaFeO_3)_2$ superlattice ($N_{BFO}/N_{tot} = 0.66$) with tilt pattern $a^-a^-c^+$. The octahedra are labeled as in Table IV.

Octahedron	Angle x	Angle y	Angle z
1 (BFO)	10.6	10.5	11.0
2 (BFO)	10.6	10.5	11.0
3 (BFO)	10.6	8.7	11.0
4 (interface)	10.1	9.9	9.3
5 (LFO)	9.2	9.1	7.6
6 (interface)	10.1	9.9	9.3

TABLE VI. Rotation angles in the $(BiFeO_3)_3/(LaFeO_3)_1$ superlattice ($N_{BFO}/N_{tot} = 0.75$) with tilt pattern $a^-a^-c^+$. The octahedra are labeled as in Table IV.

Octahedron	Angle x	Angle y	Angle z
1 (BFO)	10.6	10.5	11.0
2 (BFO)	10.6	10.5	11.0
3 (interface)	10.0	9.9	9.2
4 (interface)	10.0	9.9	9.2

TABLE VII. Rotation angles in the $(BiFeO_3)_5/(LaFeO_3)_1$ superlattice ($N_{BFO}/N_{tot} = 0.83$). The rotations about x and y are in antiphase. The rotation angles about z are reported with their sign, showing that the tilt pattern is not purely in-phase nor purely antiphase. The octahedra are labeled as in Table IV.

Octahedron	Angle x	Angle y	Angle z
1 (BFO)	8.6	8.4	+10.9
2 (BFO)	8.8	8.6	−7.9
3 (BFO)	8.6	8.5	−11.0
4 (BFO)	8.2	8.1	+7.0
5 (interface)	8.3	7.9	−10.6
6 (interface)	8.0	7.6	+0.5

TABLE VIII. Rotation angles in bulk $BiFeO_3$ and $LaFeO_3$ strained to $DyScO_3$ in the $R3c$ ($a^-a^-a^-$) and in the $Pnma$ ($a^-a^-c^+$) phases.

	Angle x	Angle y	Angle z
BFO $a^-a^-a^-$	8.4	8.1	8.6
BFO $a^-a^-c^+$	10.6	10.5	10.9
LFO $a^-a^-a^-$	7.6	7.4	8.8
LFO $a^-a^-c^+$	9.4	9.2	8.0

a large region of coexistence, while the boundary between the intermediate and the $LaFeO_3$-like phases is less well defined due to the absence of sharp contrast in the average lattice parameter. However, when temperature dependence is taken into account, it becomes clear that $BiFeO_3$ fraction as a single parameter no longer adequately describes the complex behavior of the system. Rather, the transition from the $BiFeO_3$-like phase to the high temperature (paraelectric) phase is sharp and scales with the thickness of the $BiFeO_3$ layer in a period as shown in Fig. 7(b).

If we compare these observations to the phase diagrams obtained from solid solutions [20,21,26,37], we see that the overall features and also the position of the boundaries are similar. These similarities and the fact that, even in the short period superlattices, the high density of interfaces between the two component materials does not appear to play a significant role, unlike that observed in the $PbTiO_3/SrTiO_3$ system [1,2], suggest the overall $BiFeO_3$ fraction is the key parameter controlling the superlattice behavior. However, there are subtle differences in the structure observed in the intermediate region, ranging from an incommensurate $Imma$ phase [21] through an orthorhombic $Pbam$ phase with modulated antipolar ordering [26], to a $PbZrO_3$-like structure [37], while first-principles theory finds it impossible to distinguish among different equally stable orthorhombic structures that can be either paraelectric ($Pnma$) or polar ($Pna2_1$) [24]. Our observation of complex/mixed behavior in this region may thus be consistent with a competition between some of these structures, driven by substitution with a same-sized central ion. Moreover, the specific boundary conditions imposed by the superlattice may stabilize other structures in the phase diagram. Since the energy difference between the various phases observed in the solid solutions is believed to be quite small [24], and since we have first-principles indications that longer-period structures [34] may be competitive in superlattices of intermediate compositions, this may also explain some of the sample-to-sample variation during our study. Control of these competing phases could provide a route for the design of high-response artificial materials.

Finally, the $BiFeO_3$-thickness dependent scaling of the sharp transition from the $BiFeO_3$-like phase to the high temperature (paraelectric) phase suggests that the polarization in the $BiFeO_3$ layers does not couple through intergrown $LaFeO_3$, implying that the energy cost of polarizing $LaFeO_3$ is too high. However, such decoupling of the $BiFeO_3$ layers does offer intriguing possibilities for studying ferroelectric size effects in $BiFeO_3$, in particular since the superlattices show improved leakage properties over pure $BiFeO_3$ thin films.

ACKNOWLEDGMENTS

The authors thank P. Zubko for useful discussions and M. Lopes and S. Muller for technical support. This work was supported by the European commission FP7 project OxIDes. G.R., B.Z., and P.P. acknowledge Swiss National Science Foundation support through the NCCR MaNEP. Z.Z. acknowledges EC support under the Marie-Curie fellowship (PIEF-Ga-2011-300036). J.I. acknowledges the support of MINECO-Spain (Grants No. MAT2010-18113 and No. CSD2007-00041). Ph.G. acknowledges a Research Professorship from the Francqui Foundation.

APPENDIX: OXYGEN OCTAHEDRA ROTATION ANGLES

In this Appendix we include the details of the rotations of the oxygen octahedra for the computed superlattices. We report rotation angles for each of the octahedra of the unit cell, as they change for each layer of the superlattice. For $BiFeO_3$ contents below 80% the SLs relax in a tilt pattern consisting of antiphase rotations about x and y and in-phase rotations about z, and we use the notation $a^-a^-c^+$ to describe this phase (Tables IV–VI). The octahedra are labeled starting with the bottom $BiFeO_3$ layer, and ending with the last octahedron at the "top" interface between $LaFeO_3$ and $BiFeO_3$. For $BiFeO_3$ content larger than 80% the SLs (Table VII) relax in structure with mixed in-phase and antiphase rotations about z. The rotations about x and y are still in antiphase.

For comparison, the rotation angles of bulk $BiFeO_3$ and $LaFeO_3$ strained to $DyScO_3$ in the $R3c$ ($a^-a^-a^-$) and in the $Pnma$ ($a^-a^-c^+$) phases are reported in Table VIII).

[1] M. Dawber, C. Lichtensteiger, M. Cantoni, M. Veithen, P. Ghosez, K. Johnston, K. M. Rabe, and J.-M. Triscone, Phys. Rev. Lett. **95**, 177601 (2005).

[2] M. Dawber, N. Stucki, C. Lichtensteiger, S. Gariglio, P. Ghosez, and J. M. Triscone, Adv. Mater. **19**, 4153 (2007).

[3] N. A. Pertsev, P.-E. Janolin, J.-M. Kiat, and Y. Uesu, Phys. Rev. B **81**, 144118 (2010).

[4] R. Ranjith, B. Kundys, and W. Prellier, Appl. Phys. Lett. **91**, 222904 (2007).

[5] R. Ranjith, W. Prellier, J. W. Cheah, J. Wang, and T. Wu, Appl. Phys. Lett. **92**, 232905 (2008).

[6] J. L. Blok, D. H. A. Blank, G. Rijnders, K. M. Rabe, and D. Vanderbilt, Phys. Rev. B **84**, 205413 (2011).

[7] E. Bousquet, M. Dawber, N. Stucki, C. Lichtensteiger, P. Hermet, S. Gariglio, J.-M. Triscone, and P. Ghosez, Nature (London) **452**, 732 (2008).

[8] A. Y. Borisevich, H. J. Chang, M. Huijben, M. P. Oxley, S. Okamoto, M. K. Niranjan, J. D. Burton, E. Y. Tsymbal, Y. H. Chu, P. Yu, R. Ramesh, S. V. Kalinin, and S. J. Pennycook, Phys. Rev. Lett. **105**, 087204 (2010).

[9] P. Zubko, N. Jecklin, A. Torres-Pardo, P. Aguado-Puente, A. Gloter, C. Lichtensteiger, J. Junquera, O. Stéphan, and J.-M. Triscone, Nano Lett. **12**, 2846 (2012).

[10] V. A. Stephanovich, I. A. Lukyanchuk, and M. G. Karkut, Phys. Rev. Lett. **94**, 047601 (2005).

[11] P. Aguado-Puente and J. Junquera, Phys. Rev. B **85**, 184105 (2012).

[12] Z. Zanolli, J. C. Wojdel, J. Íñiguez, and Ph. Ghosez, Phys. Rev. B **88**, 060102(R) (2013).

[13] Y. Jia, J. Solid State Chem. **95**, 184 (1991).

[14] G. Catalan and J. F. Scott, Adv. Mater. **21**, 2463 (2009).

[15] F. Kubel and H. Schmid, Acta Crystallogr., Sect. B: Struct. Sci. **46**, 698 (1990).

[16] A. M. Glazer, Acta Crystallogr., Sect. B: Struct. Crystallogr. Cryst. Chem. **28**, 3384 (1972).

[17] M. Marezio and P. Dernier, Mater. Res. Bull. **6**, 23 (1971).

[18] A. V. Zaleskii, A. A. Frolov, T. A. Khimich, and A. A. Bush, Phys. Solid State **45**, 141 (2003).

[19] H. Béa, M. Bibes, F. Ott, B. Dupé, X.-H. Zhu, S. Petit, S. Fusil, C. Deranlot, K. Bouzehouane, and A. Barthélémy, Phys. Rev. Lett. **100**, 017204 (2008).

[20] D. Kan, C.-J. Cheng, V. Nagarajan, and I. Takeuchi, J. Appl. Phys. **110**, 014106 (2011).

[21] D. A. Rusakov, A. M. Abakumov, K. Yamaura, A. A. Belik, G. Van Tendeloo, and E. Takayama-Muromachi, Chem. Mater. **23**, 285 (2011).

[22] C. M. Kavanagh, R. J. Goff, A. Dauod-Aladine, P. Lightfoot, and F. D. Morrison, Chem. Mater. **24**, 4563 (2012).

[23] Z. V. Gabbasova, M. D. Kuz'min, A. K. Zvezdin, I. S. Dubenko, V. A. Murashov, D. N. Rakov, and I. B. Krynetsky, Phys. Lett. A **158**, 491 (1991).

[24] O. E. González-Vázquez, J. C. Wojdel, O. Diéguez, and J. Íñiguez, Phys. Rev. B **85**, 064119 (2012).

[25] G. Le Bras, P. Bonville, D. Colson, A. Forget, N. Genand-Riondet, and R. Tourbot, Physica B: Condens. Matter **406**, 1492 (2011).

[26] I. O. Troyanchuk, D. V. Karpinsky, M. V. Bushinsky, V. A. Khomchenko, G. N. Kakazei, J. P. Araujo, M. Tovar, V. Sikolenko, V. Efimov, and A. L. Kholkin, Phys. Rev. B **83**, 054109 (2011).

[27] G. Kresse and J. Furthmüller, Phys. Rev. B **54**, 11169 (1996).

[28] G. Kresse and D. Joubert, Phys. Rev. B **59**, 1758 (1999).

[29] J. P. Perdew, A. Ruzsinszky, G. I. Csonka, O. A. Vydrov, G. E. Scuseria, L. A. Constantin, X. Zhou, and K. Burke, Phys. Rev. Lett. **100**, 136406 (2008).

[30] A. I. Liechtenstein, V. I. Anisimov, and J. Zaanen, Phys. Rev. B **52**, R5467 (1995).

[31] L. Pintilie, K. Boldyreva, M. Alexe, and D. Hesse, New J. Phys. **10**, 013003 (2008).

[32] D. Kan, L. Pálová, V. Anbusathaiah, C.-J. Cheng, S. Fujino, V. Nagarajan, K. M. Rabe, and I. Takeuchi, Adv. Funct. Mater. **20**, 1108 (2010).

[33] K. M. Rabe, in *Functional Metal Oxides: New Science and Novel Applications*, edited by S. B. Ogale, T. Venkatesan, and M. Blamire (Wiley, New York, 2013).

[34] S. Prosandeev, D. Wang, W. Ren, J. Íñiguez, and L. Bellaiche, Adv. Funct. Mater. **23**, 234 (2013).

[35] E. A. Eliseev, S. V. Kalinin, Y. Gu, M. D. Glinchuk, V. Khist, A. Borisevich, V. Gopalan, L. Q. Chen, and A. N. Morozovska, Phys. Rev. B **88**, 224105 (2013).

[36] D. C. Arnold, K. S. Knight, F. D. Morrison, and P. Lightfoot, Phys. Rev. Lett. **102**, 027602 (2009).

[37] J. Bielecki, P. Svedlindh, D. T. Tibebu, S. Cai, S.-G. Eriksson, L. Börjesson, and C. S. Knee, Phys. Rev. B **86**, 184422 (2012).